CrossMark

Catalyst-free growth and tailoring morphology of zinc oxide nanostructures by plasma-enhanced deposition at low temperature

W. Z. Chen · B. B. Wang · Y. Z. Qu · X. Huang ·
K. Ostrikov · I. Levchenko · S. Xu · Q. J. Cheng

Abstract ZnO nanostructures were grown under different deposition conditions from Zn films pre-deposited onto Si substrates in O_2-Ar plasma, ignited in an advanced custom-designed plasma-enhanced horizontal tube furnace deposition system. The morphology and structure of the synthesized ZnO nanostructures were systematically and extensively investigated by scanning and transmission electron microscopy, Raman spectroscopy, and atomic force microscopy. It is shown that the morphology of ZnO nanostructures changes from the hybrid ZnO/nanoparticle and nanorod system to the mixture of ZnO nanosheets and nanorods when the growth temperature increases, and the density of ZnO nanorods increases with the increase of oxygen flow rate. The formation of ZnO nanostructures was explained in terms of motion of Zn atoms on the Zn nanoparticle surfaces, and to the local melting of Zn nanoparticles or nanosheets. Moreover, the photoluminescence properties of ZnO nanostructures were studied, and it was revealed that the photoluminescence spectrum features two strong ultraviolet bands at about 378 and 399 nm and a series of weak blue bands within a range of 440–484 nm, related to the emissions of free excitons, near-band edge, and defects of ZnO nanostructures. The obtained results enrich our knowledge on the synthesis of ZnO-based nanostructures and contribute to the development of ZnO-based optoelectronic devices.

W. Z. Chen
Key Laboratory of Information Functional Material for Fujian Higher Education, College of Physics & Information Engineering, Quanzhou Normal University, Quanzhou 362000 Fujian, People's Republic of China

B. B. Wang
College of Chemical Engineering, Chongqing University of Technology, Chongqing 400054, People's Republic of China

Y. Z. Qu · X. Huang · Q. J. Cheng (✉)
College of Energy, Xiang'an Campus, Xiamen University, Xiamen 361102 Fujian, People's Republic of China
e-mail: qijin.cheng@xmu.edu.cn

K. Ostrikov
School of Chemistry, Physics and Mechanical Engineering, Queensland University of Technology, Brisbane 4000, Australia

K. Ostrikov
CSIRO-QUT Joint Sustainable Processes and Devices Laboratory, Commonwealth Scientific and Industrial Research Organization, P.O. Box 218, Lindfield, NSW 2070, Australia

I. Levchenko · S. Xu
Plasma Sources and Applications Centre, National Institute of Education, Nanyang Technological University, 1 Nanyang Walks, Singapore 637616, Singapore

I. Levchenko
School of Chemistry, Physics and Mechanical Engineering, Queensland University of Technology, Brisbane 4000, Australia

Introduction

ZnO is a compound direct band gap semiconductor with a wide band gap of 3.37 eV and a high exciton energy of 60 meV at room temperature (Ostrikov et al. 2013; Zhang et al. 2009; Wang 2004; Yin et al. 2016). It is a very promising material for microelectronic and optoelectronic devices, photocatalysis, piezoelectric transducers, chemical sensors, and many other advanced techniques (Cheng et al. 2012; Nipane et al. 2015; Han et al. 2010; Shirolkar et al. 2013). In the form of nanostructures, ZnO is especially attractive for the advanced applications. Due to their outstanding properties such as high surface area to volume ratio, high length to diameter ratio, unique morphology and perfect crystalline structure, the low-dimensional ZnO nanostructures become a spotlight of extensive research efforts (Ostrikov et al. 2013; Cheng et al. 2011; Huang et al. 2012; Greenberg et al. 2015; Raffone et al. 2016). Moreover, properties of ZnO nanostructures can be effectively tuned by changing their structure and morphology. For example, the conductivity of ZnO nanobelts changes with their surface area and level of oxygen deficiency (Wang 2004). Another example is the alteration of photoluminescence properties by changing the surface roughness of ZnO nanorods (Zhu et al. 2011).

To date, ZnO nanostructures have been successfully synthesized by various methods such as liquid-based technique, sputtering, evaporation and chemical vapor deposition (CVD), and many others (Zhang et al. 2009; Zhu et al. 2011; Mbuyisa et al. 2012; Podrezova et al. 2013). Particularly, the CVD method is widely employed to synthesize various ZnO morphologies such as awl-like ZnO nanostructures (Cai et al. 2014), nanorods (Trevizo et al. 2015), nanowires (Lu et al. 2012), etc. However, ZnO nanostructures are mainly grown at high (typically exceeding 900 °C) temperatures in the catalytic CVD process (Cai et al. 2014; Trevizo et al. 2015; Lu et al. 2012), and this potentially deteriorates the properties of outcome nanostructures and efficiency of the whole process.

Can the ZnO nanostructures be prepared *at low temperature and without catalyst*? Low-temperature catalyst-free technique could significantly reduce the cost due to saving energy and precursor materials. Furthermore, the low-temperature catalyst-free technique is environment-friendly due to reduced heat and chemicals release to atmosphere.

How to turn this technique into reality? This work aims to synthesize the ZnO nanostructures using the low-temperature catalyst-free technique.

In this work, Zn films pre-deposited onto Si substrates by magnetron sputtering were oxidatively treated with O_2-Ar plasma in an advanced custom-made plasma-enhanced horizontal tube furnace deposition system to realize the growth of ZnO nanostructures free of catalyst at low (up to 550 °C) temperature. Moreover, by tailoring the process parameters (including growth temperature and gas flow rates of Ar and O_2, etc.), morphology of ZnO nanostructures was tuned in a wide range from the hybrid of ZnO nanoparticles and nanorods to the mixture of ZnO nanosheets and nanorods.

We have also proposed a plausible mechanism to interpret the morphology change in terms of the atomic motion of Zn atoms on the surface of Zn nanoparticles and the local melting of Zn nanoparticles or nanosheets during the growth. Furthermore, considering the application of ZnO nanostructures in the field of optoelectronics, their photoluminescence property was also investigated.

This paper is structured as follows. In the "Method and experimental overview" section, we present the details of the experimental method and the characterization techniques. The effect of the substrate temperature and oxygen gas flow rate on the morphological, structural, and optical properties of the synthesized ZnO nanostructures and the discussion of the possible physical plasma-related mechanisms that explain the obtained experimental results are presented in the "Results and Discussion" section. This paper ends with a short summary in the "Conclusions" section.

Method and experimental overview

Low-dimensional ZnO nanostructures were synthesized by exposing Zn films pre-deposited onto silicon substrates to the O_2-Ar plasma in the plasma-enhanced horizontal tube furnace deposition system. Prior to the deposition of Zn films, the silicon substrates were cleaned for 15 min by ultrasonication in the solution of acetone, alcohol, and deionized water. Thereafter, a layer of Zn film of approximately 1000 nm was deposited after ultrasonic cleaning onto the clean silicon substrates by radio frequency (RF) magnetron sputtering in the Ar plasma at a pressure of 7 mtorr, RF power of 30 W, and sputtering time of 10 min.

The synthesis of ZnO nanostructures was then carried out in an advanced custom-made plasma-enhanced horizontal tube furnace deposition system shown in Fig. 1. In this setup, we have used two stainless steel
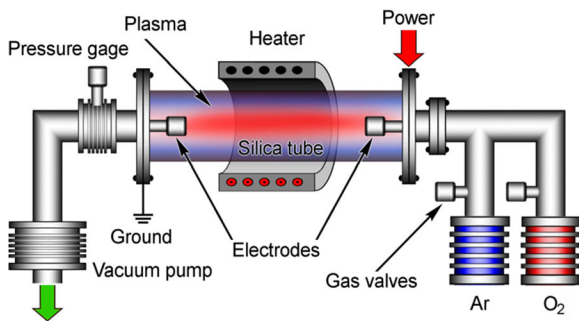
Fig. 1 Schematic of plasma-enhanced horizontal tube furnace deposition system. Gas is supplied to silica tube, where discharge is sustained due to voltage applied across electrodes installed in the opposite lids

electrodes installed at both sides of the silica tube, while the RF power with a frequency of 40 kHz was supplied to these electrodes. This configuration is capable to produce the low-temperature plasma along the whole silica tube. The length and diameter of the tube were 1200 and 60 mm, respectively. A heater installed outside the tube was used to heat the substrate and reactive gases. The pressure in the reactor can be adjusted by the gas valves monitored by the pressure gages.

At the initial stage of the process, silicon substrates with pre-deposited Zn film were placed in the middle of the silica tube, and the reactor was evacuated to a base pressure lower than 10 Pa. Then, Ar gas was supplied into the reactor and simultaneously, the heater was switched on. When the substrate temperature reached the targeted growth temperature, O_2 gas was also supplied into the reactor. After reaching the stable working pressure by adjusting vacuum valves, the radio frequency power supply was turned on to ignite a plasma, and the growth of ZnO nanostructures was started.

Specifically, eight samples were prepared according to the growth conditions listed in Table 1. For samples

A–E, the substrate temperature ranged from 350 to 550 °C, whereas the Ar and O_2 gas flow rates, total gas working pressure, RF power, and deposition time were kept constant at 40 sccm (cubic centimeter per minute at STP), 11 sccm, 150 Pa, 66 W, and 10 min, respectively. For samples F–H, the O_2 gas flow rate was increased from 5 to 45 sccm (the working pressure changed from 125 to 195 Pa correspondingly), while the Ar gas flow rate, substrate temperature, RF power, and deposition time were kept constant at 40 sccm, 450 °C, 66 W, and 10 min, respectively.

The morphology and structure of the synthesized samples were studied using SU70 scanning electron microscope (SEM) operated at 15 kV, X'pert PRO X-ray diffractometer (XRD), F30 FEG transmission electron microscope (TEM) operated at 200 kV, and Witec alpha 300 Raman spectroscope using the laser with a wavelength of 532 nm as the excitation source. The elemental composition of ZnO nanostructures was assessed using an Oxford Instruments EDX INCA spectrometer coupled to SU70 SEM. The surface topography of these ZnO nanostructures was studied using atomic force microscopy (AFM) (Nanoscope IIIa, digital scanning). The photoluminescence (PL) properties of ZnO nanostructures were measured in HitachiF-7000 system using the laser with a wavelength of 350 nm as the excitation source.

Results and discussion

Structure and composition of ZnO nanostructures

Figure 2 shows the cross-sectional SEM images of Zn films grown on the silicon substrates, before and after heating. As seen from Fig. 2a, the as-prepared Zn film

Table 1 Growth parameters including Ar and O_2 gas flow rates, working pressure, growth temperature (T), RF power (P), and deposition time (t)

Sample	Ar (sccm)	O_2 (sccm)	Pressure (Pa)	T (°C)	P (W)	t (min)
A	40	11	150	350	66	10
B	40	11	150	400	66	10
C	40	11	150	450	66	10
D	40	11	150	500	66	10
E	40	11	150	550	66	10
F	40	5	125	450	66	10
G	40	25	170	450	66	10
H	40	45	195	450	66	10

before heating is composed of Zn nanoparticles. On the other hand, Fig. 2b, c shows that Zn nanowires and nanosheets are present in the samples heated to 400 °C (the thickness of the ZnO nanostructures grown at 400 °C is approximately 1066 nm), whereas only nanosheets are found in samples heated to 500 °C (the thickness of the ZnO nanostructures grown at 500 °C is approximately 1433 nm). Thus, Fig. 2b, c evidences the change of Zn film morphology from structures composed mostly of nanoparticles to the arrays of nanowires and nanosheets with the increase of processing temperature.

Figure 3 shows the SEM images of samples **a**–**e** grown at different temperatures ranging from 350 to 550 °C. Interestingly, the morphology of the ZnO nanostructures changes with the increase of the growth temperature from hybrid structure of nanoparticles and nanorods to the mixture of nanosheets and nanorods.

Figure 4 is the XRD spectra of samples (*a*–*e*). The peaks at about 32°, 34.86°, 36.59°, 47.85°, and 56.9° are assigned to the diffraction of ZnO (JCPDS card, No. 65-3411), whereas the peaks at about 43.67° and 54.84° originate from the diffraction of Zn (JCPDS card, No.65-3358). The mean grain size corresponding to the (002) crystal plane of ZnO nanostructures synthesized at different growth temperatures has been calculated using the Debye-Scherrer formula ($d = 0.9\lambda/B \cos\theta$, where d is the mean grain size of the ZnO nanostructures, λ is the incident wavelength of X-ray radiation, B is the full width at half maximum of the diffraction peak, and θ is the Bragg diffraction angle, respectively). The calculated mean grain size d is shown

in Table 2. From Table 2, one can see that d increases from 18.0 to 45.6 nm with the growth temperature increasing from 350 to 550° C; this means that the increased substrate temperature promotes the motion of Zn atoms on the surface and growth of ZnO nanostructures. From Fig. 4, one also can notice that the diffraction peaks attributed to Zn disappear in spectra (*c*)–(*e*), indicating a residual Zn in the samples grown at low temperatures of 350 and 400 °C.

Figure 5 shows the SEM images of samples F–H (Table 1) grown under different flow rates of O_2. From this figure, one can notice that the number of nanorods was enhanced with the increase of the oxygen flow rate.

Figure 6a displays the XRD spectra of samples F–H. The peaks at about 32°, 34.87°, 36.68°, 47.86°, and 56.9° originate from the diffraction of ZnO (JCPDS card, No. 65-3411), and the peak at about 43.52° is attributed to the diffraction of Zn (JCPDS card, No. 65-3358) (Cheng et al. 2012; Cheng et al. 2011; Hu et al. 2007). The mean grain size d corresponding to the (002) crystal plane of ZnO nanostructures synthesized at different flow rates of O_2 has also been calculated using the Debye-Scherrer formula. The estimated mean grain sizes are listed in Table 3. As the gas flow rate of O_2 increases from 5 to 45 sccm, the mean grain size increases from 27.3 to 38.1 nm. The increased mean grain size with the increase of gas flow rate of O_2 possibly originates from the enhanced nucleation rate at a high gas flow rate of O_2. In addition, the diffraction peak at about 33.38° originates from crystal Si (JCPDS card, No.40-0932).

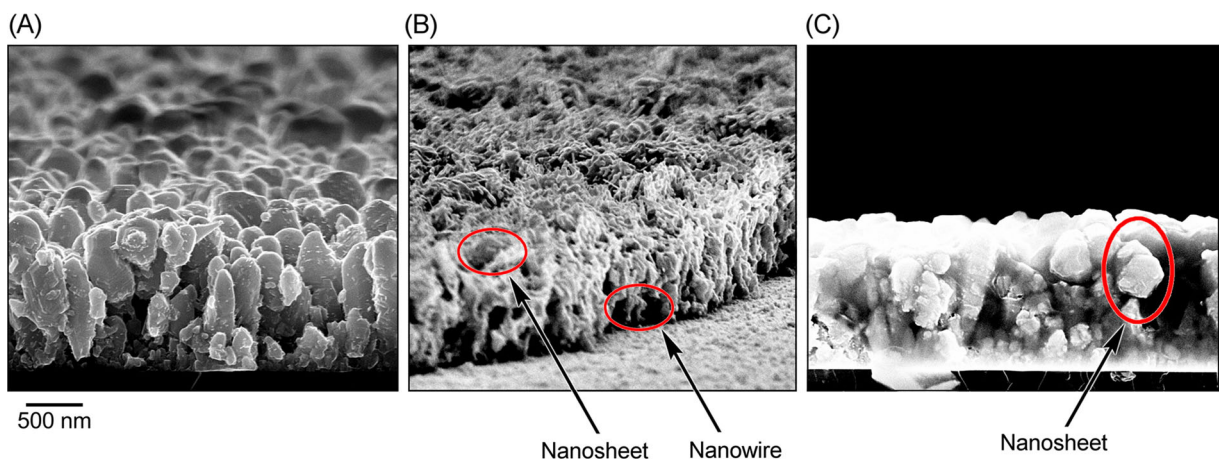Nanosheet   Nanowire

Nanosheet

Fig. 2 Cross-sectional SEM images of Zn films before and after heating. **a** As-deposited Zn film consisting of nanoparticles. **b** Zn film consisting of nanowires and nanosheets after heating to 400 °C. **c** Only nanosheets are present in the structure after heated to 500 °C. Scale bar is 500 nm for all panels
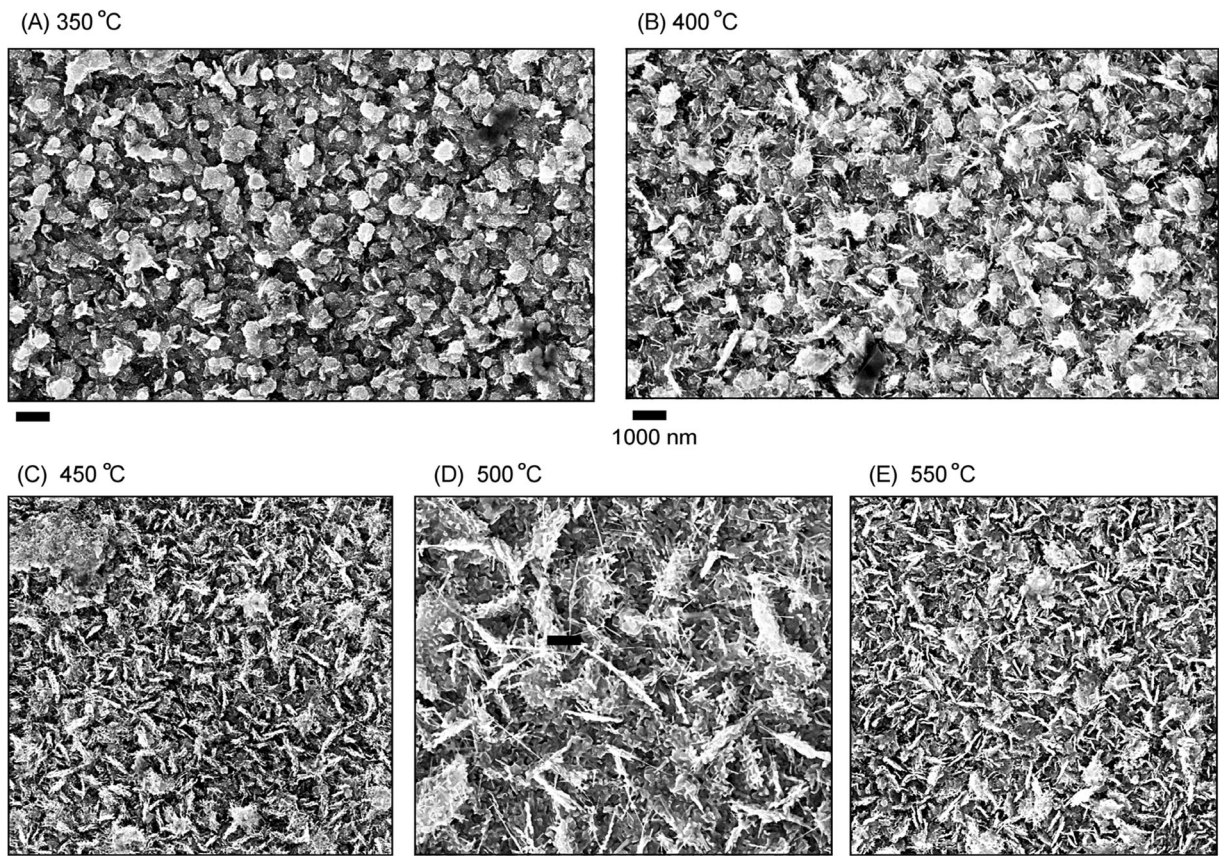
(A) 350 °C

(B) 400 °C

1000 nm

(C) 450 °C

(D) 500 °C

(E) 550 °C

Fig. 3 SEM images of the ZnO nanostructures grown at different temperatures ranging from 350 to 550 °C. Increase of the growth temperature results in the morphology change from hybrid nanoparticle/nanorods to structure (**a**) to the mixture of nanosheets and nanorods (**d**, **e**). Scale bars are 1000 nm for all samples

Figure 6b shows a typical Raman spectrum of sample C. As it is seen, the Raman peak at about 433.5 cm^{-1} is attributed to the E_2 (high) mode of ZnO (Kerr et al. 2007; Hsu et al. 2012), which is the characteristic peak of wurtzite hexagonal phase of ZnO (Mbuyisa et al. 2012).
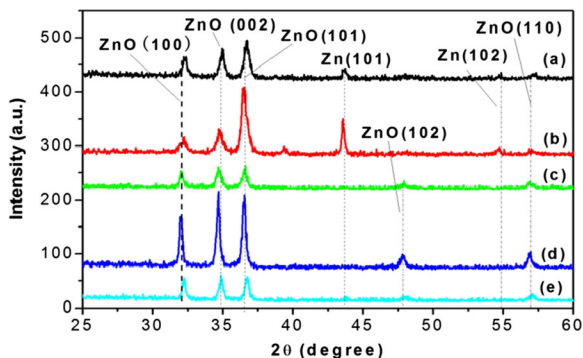
The Raman peak at about 194.1 cm^{-1} can be assigned to the E_2 (low) mode of ZnO (Zhang et al. 2009; Rajalakshmi et al. 2000). In addition, the Raman peak at about 546.9 cm^{-1} originates from a multi-phonon process of ZnO nanomaterials (Reyes et al. 2010). The Raman result further indicates that the synthesized ZnO nanostructures feature the wurzite structure.

Figure 7a shows a representative TEM image of sample H. From this image, one can notice that the diameter of a single ZnO nanorod is approximately 50 nm, and that the tip of the ZnO nanorod is smooth and flat. It needs to be pointed out that no metal particles

Fig. 4 XRD spectra of the ZnO nanostructures (*a*)–(*e*) (Ref. Fig. 3), grown at different temperatures ranging 350 to 550 °C. Diffraction peaks attributed to Zn disappear in spectra (*c*)–(*e*)

Table 2 Calculated mean grain size (*d*) for the (002) crystal plane of ZnO nanostructures synthesized at different growth temperatures (*T*) using the Debye-Scherrer formula

T (°C)	350	400	450	500	550
d (nm)	18.0	29.6	34.9	44.2	45.6

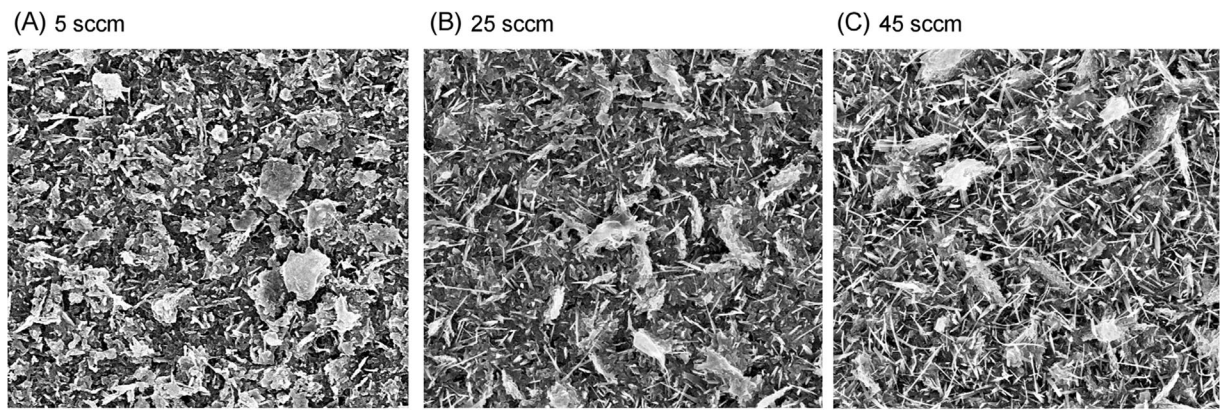(A) 5 sccm   (B) 25 sccm   (C) 45 sccm

Fig. 5 SEM images of of the ZnO nanostructures grown at different flow rates of O2 ranging from 5 to 45 sccm. Scale bars are 1000 nm for all samples. The number of nanorods increases with the increase of oxygen flow rate

have been detected at the tips of the ZnO nanostructures.

Figure 7b is a typical high-resolution TEM image of the ZnO nanorod collected from sample H. The synthesized nanorods feature a single-crystalline structure (no twin defects or screw dislocations are found in the observed area). Moreover, we have used Digital Micrograph software to obtain the width of ten layers of ZnO nanostructures, and the results are shown in Fig. 7c, d. According to the calculated width value, the average spacing between the adjacent layers is about 0.2458 nm, which corresponds to the spacing of (002) plane of ZnO (Doan et al. 2014). This finding suggests that the ZnO nanorods have a preferential growth along the (001) direction (Zhang et al. 2009).

Figure 8 shows a typical energy-dispersive X-ray (EDX) measurement of the ZnO nanostructures collected from sample C. EDX reveals that the synthesized ZnO nanostructures consist of Zn and O with an elemental composition of 57.1 and 42.9 at.%, respectively.

Figure 9 shows the surface topography of samples H and C obtained with AFM. One can notice that the diameter of sample C is much larger than that of sample H. The average surface roughness estimated was 234 and 151 nm for sample H and sample C, respectively. This result is consistent with SEM analysis.

Formation of ZnO nanostructures

Figure 2 evidences that the morphology of Zn nanoparticles gradually transforms into nanosheets with the increase of the process temperature. This effect could be explained in terms of enhancement of Zn atom diffusion on the surface of Zn nanoparticles with the temperature (Yuvaraj et al. 2009). Indeed, Figs. 3 and 5 make it possible to suppose that the ZnO nanostructures originate from Zn nanoparticles and nanosheets, thus suggesting that the ZnO nanostructures nucleate on Zn nanoparticles and
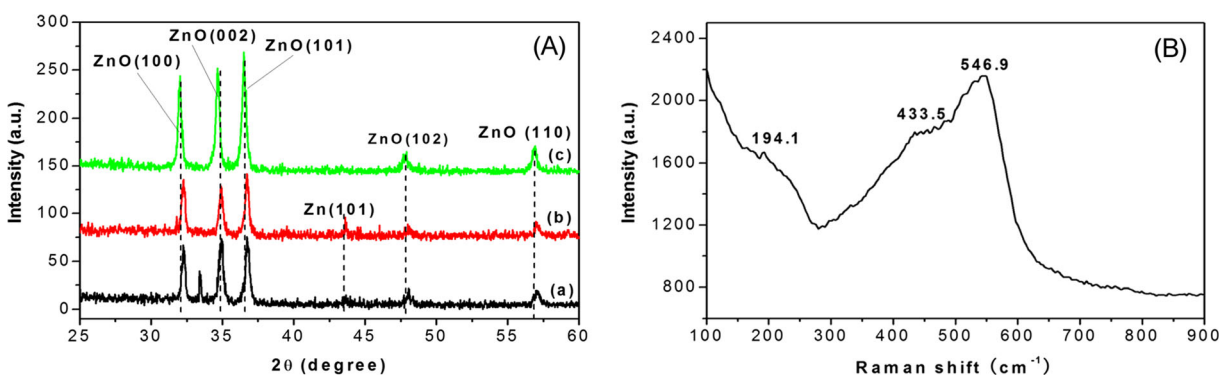

Fig. 6 **a** XRD spectra of samples grown under oxygen flow rates of 5 sccm (*a*), 25 sccm (*b*), and 45 sccm (*c*). **b** Raman spectrum of sample C

Table 3 Calculated mean grain size (d) for the (002) crystal plane of ZnO nanostructures synthesized at different flow rates of O_2 using the Debye-Scherrer formula

O_2 (sccm)	5	25	45
d (nm)	27.3	36.5	38.1

nanosheets. The schematic mechanism of the plausible ZnO nanostructure formation mechanism is shown in Fig. 10.

We should stress that the formation of volatile gaseous phase of Zn vapor followed by its high-temperature oxidation in the gas phase is one of the important contributors to the growth of ZnO nanostructures. Specifically, since the evaporation of Zn occurs at about 460 °C, small Zn nanoparticles evaporate during the process of heating the substrate due to the high surface energy of nanoparticles (Zoestbergen et al. 2013). After
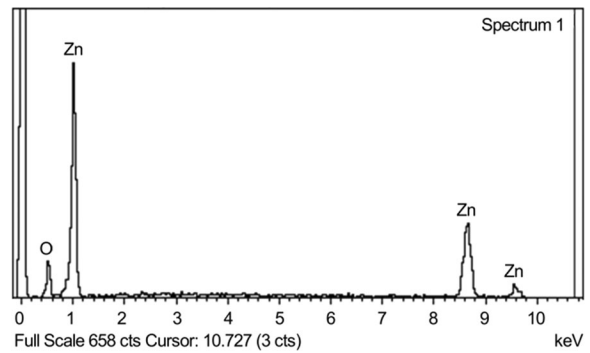

Fig. 8 EDX spectrum of sample C. The synthesized ZnO nanostructures consist of Zn and O with an elemental composition of 57.1 and 42.9 at.%

ignition of the O_2-Ar plasma, O_2 molecules are ionized into various oxygen ions such as O^+, O_2^+, and O_3^+ (Ostrikov et al. 2010; Cvelbar et al. 2012). Since gases are not completely ionized in the low-temperature
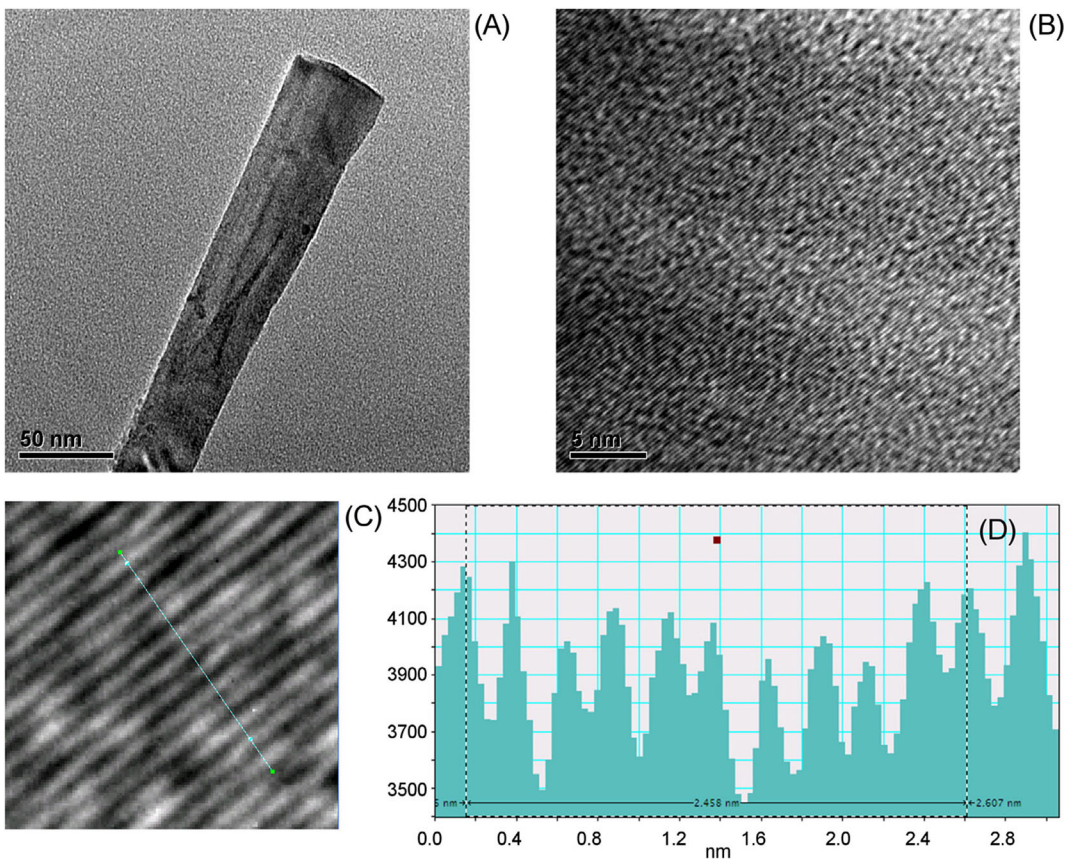

Fig. 7 Plane-view TEM (**a**) and HRTEM (**b**) images of sample H; the image (**c**) and corresponding distribution (**d**) of ten layers of ZnO nanostructures. The nanorods feature an excellent single-crystalline structure (no crystal defects such as twin defects or screw dislocations are found in the synthesized nanostructures). The average spacing between the adjacent layers is about 0.2458 nm, which corresponds to the spacing of (002) plane of ZnO
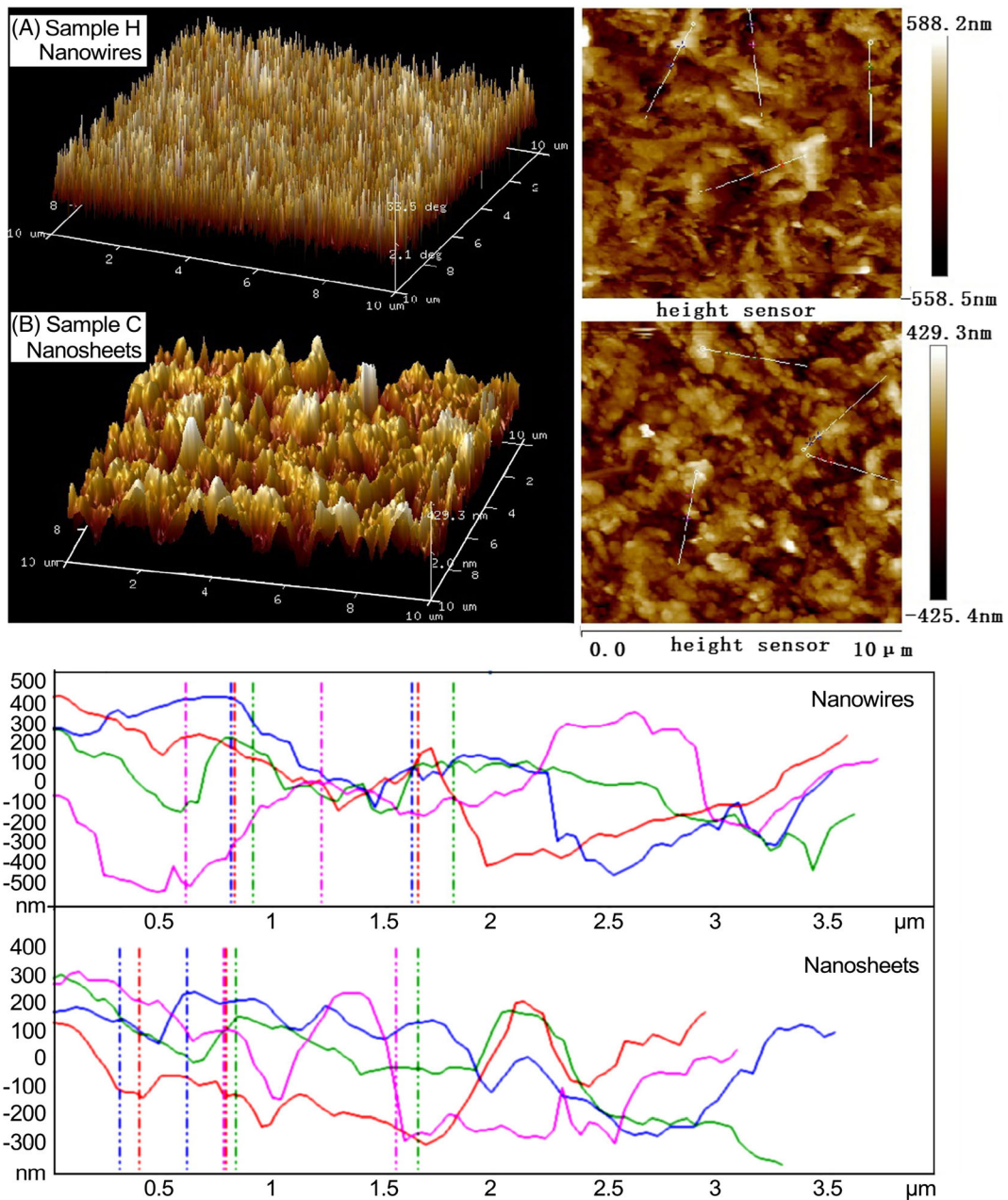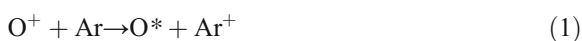
Fig. 9 AFM microgaphs of samples H (**a**) and C (**b**). The mean diameter of sample C is much larger than that of sample H. The average surface roughness (profiles shown in lower panel) estimated was 234 and 151 nm for samples H and C, respectively

plasma, a number of existed molecules are present there, and the reactions to occur in the gas environment are

$$O^+ + Ar \rightarrow O* + Ar^+ \qquad (1)$$

$$O^+ + O_2 \rightarrow O* + O_2^+ \qquad (2)$$

$$O* + Zn \rightarrow ZnO \qquad (3)$$

In Eqs. (1)–(3), O* represents the active oxygen atom. In this way, ZnO species can be formed in the gas environment and subsequently then transported to the substrate.

Formation of ZnO nanorods

Ar ions are heavy species which can efficiently sputter Zn nanoparticles and nanosheets by bombardment from the
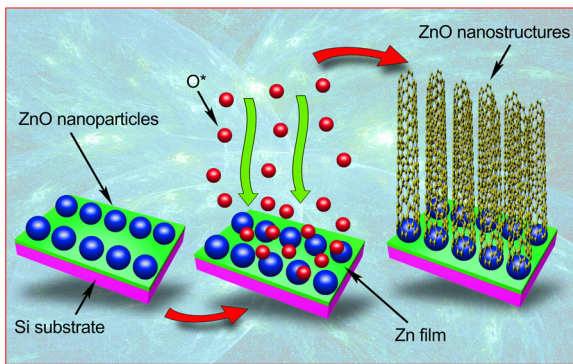
Fig. 10 Schematic of the ZnO nanostructure formation. Ar ions are heavy species which can sputter the Zn nanoparticles; hence, the pits on the surface have a high chance of being sputtered by Ar ions. As a result, the Zn microhillocks are formed. When ZnO species adsorb on the Zn microhillocks, the entropy of the system is reduced, the Zn microhillocks are locally melted, and ZnO nanorods are eventually formed

O_2-Ar plasma. The surface of formed Zn nanoparticles and nanosheets becomes rough, and hence, the pits on the surface have a high chance of being sputtered by Ar ions. As a result, Zn microhillocks are formed on the surface (Wang et al. 2009). Due to the high surface energy of Zn microhillocks, ZnO species formed in the gas environment can bond to them. When the ZnO species adsorb on the Zn microhillocks, their motion pattern changes from three dimensions to two dimensions. As a result, the entropy of the system reduces, i.e., $\Delta S < 0$. Due to the spontaneous adsorption, a change to Gibbs free energy ΔG is lower than zero. According to the formula $\Delta G = \Delta H - T\Delta S$, the enthalpy reduces, i.e., the adsorption of ZnO species is an exothermal process. Besides, the adsorption of oxygen and argon ions and the reaction of oxygen ions with Zn release some extra energy on the Zn microhillocks. Thus, the Zn microhillocks are locally melted, and the ZnO nanorods are eventually formed (Wang 2004; Ostrikov et al. 2010).

Effect of deposition parameters on the growth of ZnO nanostructures

Figure 3 shows that the ZnO nanostructure morphology changes from the hybrid ZnO nanoparticle/nanorod system to the mixture of ZnO nanosheets and nanorods when the growth temperature increases. This effect could be related to the accelerated atomic motion of Zn atoms on the surface and the enhanced reaction rate due to the increased growth temperature. When the growth temperature increases, the surface-located atoms of Zn

nanoparticles obtain sufficient energy to accelerate their atomic motion. As a result, the Zn nanoparticles are gradually transformed into planar structure due to the stable hexagonal structure of Zn (Yuvaraj et al. 2009). Due to the increase of the growth temperature, the reaction rate of Zn with oxygen is also improved, i.e., more ZnO species formed on the Zn microhillocks. On the other hand, since the wall of the tube furnace is heated, the surface temperature of silicon is higher than that of the top of Zn microhillocks. Under this circumstance, the ZnO species diffuse towards the top of Zn microhillocks and promote the growth of ZnO nanorods. As a result, the ZnO nanostructures change with the increase of the growth temperature, as shown in Fig. 3.

When the flow rate of O_2 increases, the content of oxygen in the reactor also increases. From Eqs. (1)–(3), one can see that the formation rate of ZnO species also increases in this case. As a consequence, the growth of ZnO nanorods is enhanced, and the number of ZnO nanorods increases with the increase of oxygen flow rate (as shown in Fig. 5).

PL properties of ZnO nanostructures

Figure 11 shows the photoluminescence (PL) spectrum of sample C. As shown in Fig. 11, the PL spectrum exhibits two strong PL bands located at about 378 and 399 nm and a series of weak PL bands located at about 440, 451, 468, and 484 nm. Among these bands, the PL band located at about 378 nm originates from the free exciton recombination (Zhang et al. 2009), and the PL band located at about 399 nm is attributed to the near-band edge
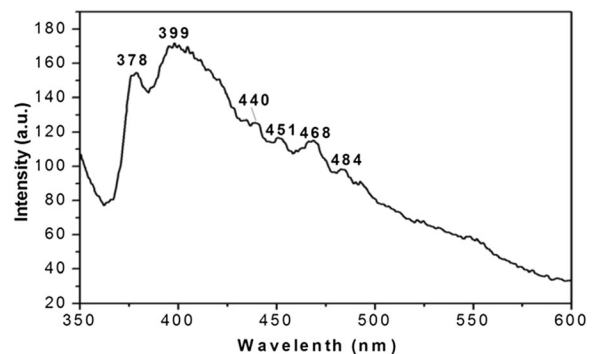

Fig. 11 Photoluminescence spectrum of sample C. The spectrum exhibits two strong bands located at about 378 and 399 nm and a series of weak bands located at about 440, 451, 468, and 484 nm

emission (Elsayed et al. 2015). The origin of weak PL bands located at about 440, 451, 468, and 484 nm is not clear, and these bands are possibly related to the defects in the ZnO nanomaterials (Chen et al. 2015; Han et al. 2010). It has been demonstrated in the previous works that (1) the peaks at ~420, ~460, ~490, and ~520 nm can be attributed to interstitial zinc (Zn_i), Zn vacancy (V_{zn}), oxygen vacancy (V_o), and oxygen antisite (O_{Zn}), respectively, and (2) the origin of yellow and orange luminescence (>540 nm) is usually attributed to oxygen interstitial (O_i) (Chen et al. 2015; Han et al. 2010). Since our EDX measurement has revealed that the synthesized ZnO nanostructures of sample C are zinc rich, the defects present in the sample possibly originate from interstitial zinc or oxygen vacancy.

Conclusions

In summary, low-dimensional ZnO nanostructures were synthesized from the pre-deposited Zn films on the Si substrates by O_2-Ar plasma in an advanced custom-designed plasma-enhanced horizontal tube furnace deposition system under different growth conditions. The results of SEM, TEM Raman, and AFM characterization have shown that the ZnO nanostructures change their morphology from the hybrid of ZnO nanoparticles and nanorods to the mixture of ZnO nanosheets and nanorods when the growth temperature increases. Moreover, the number of ZnO nanorods increases with the increase of flow rate of oxygen. In combination with the characterization results, the formation mechanism of ZnO nanostructures was investigated, which originated from the consideration of the motion of surface atoms of Zn nanoparticles and the local melting of Zn nanoparticles and nanosheets. In addition, the PL properties of ZnO nanostructures were studied, and the obtained result indicates that the ZnO nanostructures can generate two strong ultraviolet PL bands and a series of weak blue PL bands, which can be attributed to the emissions of free excitons, near-band edge, and defects of ZnO nanostructures, respectively. These results are highly relevant to the development of an advanced process for the synthesis and application of ZnO-based nanomaterials.

References

Cai X, Wang F, Yan D, Zhu Z, Gu X (2014) Luminescence characteristics and growth mechanism of awl-like ZnO nanostructures fabricated on Ni-coated silicon substrate via chemical vapor deposition method. Ceram Int 40:12293–12298

Chen HI, Hsiao JJ, Huang YJ, Wang JC, Wu YF, Lu BY, Nee T-E (2015) Strain modulated defect luminescence in ZnO nanostructures grown on Si substrates. J Lumin 168:304–308

Cheng QJ, Ostrikov K (2011) Temperature-dependent growth mechanisms of low-dimensional ZnO nanostructures. Cryst Eng Comm 13:3455–3461

Cheng QJ, Ostrikov K (2012) Property-performance control of multidimensional, hierarchical, single-crystalline ZnO nanoarchitectures. Chem Phys Chem 13:1535–1541

Cvelbar U, Chen Z, Levchenko I, Sheetz RM, Jasinski JB, Menon M, Sunkara MK, Ostrikov K (2012) Sub-oxide-to-metallic, uniformly-nanoporous crystalline nanowires by plasma oxidation and electron reduction. Chem Commun 48:11070–11072

Doan MT, Ho XV, Nguyen T, Nguyen VN (2014) Influence of doping Co to characterization of ZnO nanostructures. Adv Nat Sci: Nanosci Nanotechno 5:025011–025014

Elsayed KA, Anad NS, Fattah GA, Imam H, Kayed TS, Ismail LZ (2015) ZnO nanostructures induced by microwave plasma. Arab J Chem 8:553–559

Greenberg BL, Ganguly S, Held JT, Kramer NJ, Mkhoyan KA, Aydil ES, Kortshagen UR (2015) Nonequilibrium-plasma-synthesized ZnO nanocrystals with plasmon resonance tunable via al doping and quantum confinement. Nano Lett 15:8162–8169

Han N, Hu P, Zuo A, Zhang D, Tian Y, Chen Y (2010) Photoluminescence investigation on the gas sensing property of ZnO nanorods prepared by plasma-enhanced CVD method. Sensor Actuator B 145:114–119

Hsu NF, Chang M (2012) A study on rapid growth and piezoelectric effect of ZnO nanowires array. Mater Chem Phys 135:112–116

Hu HM, Huang XH, Deng CH, Chen XY, Qian YT (2007) Hydrothermal synthesis of ZnO nanowires and nanobelts on a large scale. Mater Chem Phys 106:58–62

Huang SY, Cheng QJ, Xu S, Wei DY, Zhou HP, Long JD, Levchenko I, Ostrikov K (2012) Self-organized ZnO nanodot arrays: effective control using SiNx interlayers and low-temperature plasmas. J Appl Phys 111:036101–036103

Kerr LL, Li X, Canepa M, Sommer AJ (2007) Raman analysis of nitrogen doped ZnO. Thin Solid Films 515:5282–5286

Lu L, Chen J, Li L, Wang W (2012) Direct synthesis of vertically aligned ZnO nanowires on FTO substrates using a CVD method and the improvement of photovoltaic performance. Nanoscale Res Lett 7:293–298

Mbuyisa P, Bhardwaj SP, Rigoni F, Carlino E, Pagliara S, Sangaletti L, Goldoni A, Ndwandwe M, Cepek C (2012) Controlled synthesis of carbon nanostructures using aligned ZnO nanorods as templates. Carbon 50:5472–5480

Nipane SV, Korake PV, Gokavi GS (2015) Graphene-zinc oxide nanorod nanocomposite as photocatalyst for enhanced degradation of dyes under UV light irradiation. Ceram Int 41: 4549–4557

Ostrikov K, Levchenko I, Cvelbar I, Sunkara I, Mozetic M (2010) From nucleation to nanowires: a single-step process in reactive plasmas. Nanoscale 2:2012–2027

Ostrikov K, Neyts EC, Meyyappan M (2013) Plasma nanoscience: from nano-solids in plasmas to nano-plasmas in solids. Adv Phys 62:113–224

Podrezova LV, Porro S, Cauda V, Fontana M, Cicero G (2013) Comparison between ZnO nanowires grown by chemical vapor deposition and hydrothermal synthesis. Appl Phys A Mater Sci Process 113:623–632

Raffone F, Risplendi F, Cicero G (2016) A new theoretical insight into ZnO NWs memristive behavior. Nano Lett 16:2543–2547

Rajalakshmi M, Arora AK, Bendre BS, Mahamuni S (2000) Optical phonon confinement in zinc oxide nanoparticles. J Appl Phys 87:2445–2445

Reyes JD, Juárez JM, García ML, Juárez G, Galeazzi R (2010) Growth and characterization of ZnO films deposited by chemical bath and annealed by microwaves (CBD-AµW). IOP Conf Series: Mater Sci Eng 12:012003–012004

Shirolkar MM, Hao C, Yin S, Li M, Wang H (2013) Influence of surface null potential on nonvolatile bistable resistive switching memory behavior of dilutely aluminum doped ZnO thin film. Appl Phys Lett 102:243501–243505

Trevizo AS, Madrid PA, Ruiz PP, Flores WA, Gutiérrez CO, Yoshida MM (2015) Single and multi-layered core-shell structures based on ZnO nanorods obtained by aerosol assisted chemical vapor deposition. Mater Charact 105:64–70

Wang BB, Ostrikov K (2009) Tailoring carbon nanotips in the plasma-assisted chemical vapor deposition: effect of the process parameters. J Appl Phys 105:083303–083309

Wang ZL (2004) Zinc oxide nanostructures: growth, properties and applications. J Phys Condens Matter 16:R829–R858

Yin S, Shirolkar MM, Li J, Li M, Song X, Dong X, Wang H (2016) Influences of defects evolvement on the properties of sputtering deposited ZnO:Al films upon hydrogen annealing. AIP Adv 6:065020–065013

Yuvaraj D, Rao KN, Barai K (2009) Synthesis of platestacks and microtowers of zinc by thermal evaporation. Solid State Commun 149:349–351

Zhang R, Yin PG, Wang N, Guo L (2009) Photoluminescence and Raman scattering of ZnO nanorods. Solid State Sci 11:865–869

Zhu K, Wang W, Chen W, Liu J, Song B, Jiang L, Guo CJ (2011) Catalyst-free synthesis of ZnO microrod arrays on SiC substrate and their tunable photoluminescence by erosion process. J Alloys Compd 509:6942–6945

Zoestbergen E, Maalman TFJ, Commandeur C, Goodenough M (2013) Influence of contamination on the thermal evaporation of a zinc melt. Surf Coat Technol 218:108–113